




DEVELOPMENTS IN THE PRODUCTION OF MAGNESIUM ALLOY FLAT PRODUCTS

Microstructural and Texture Evolution of Hot-Rolled TA32 Alloy and Its Effect on Tensile Properties

CHANDRA S. PERUGU ^{1,3} KRISHNA KAMLESH VERMA,¹
H.C. MADHU,² and PADAIKATHAN PAMBANNAN¹

1.—Department of Materials Engineering, Indian Institute of Science, Bengaluru, India.
2.—Department of Mechanical Engineering, Siddaganga Institute of Technology, Tumkuru, India.
3.—e-mail: pernish@gmail.com

A challenge for the research and industrial community is to develop light-weight wrought Mg-based alloys that exhibit high strength and good ductility. To address this challenge, Mg-3Sn-2Al (TA32) alloy was produced by the squeeze casting process followed by hot rolling (HR). To improve its ductility, the hot-rolled alloy was annealed (HRA). HR and HRA samples were subjected to microstructural, composition, textural, and mechanical property analysis. The HR sheet exhibited high strength with 0.2% proof stress (PS) of 274 MPa and ultimate tensile strength (UTS) of 390 MPa, as well as reasonable ductility (12%) along the rolling direction, one of the highest values for Mg alloys. HRA sheet showed a moderate reduction in strength with a 0.2% PS of 250 MPa and UTS of 365 MPa, but an improvement in ductility (19%). The excellent properties of this alloy can be attributed to the synergistic effects of grain refinement, solid-solution strengthening by Al and Sn atoms, and uniform distribution of fine Mg₂Sn particles.

INTRODUCTION

Rolled Mg-based alloys are especially attractive owing to their low density, high specific strength, stiffness, and recyclability. However, Mg is not satisfactorily amenable to room-temperature forming, due to its hexagonal close-packed (HCP) crystal structure that lacks independent slip systems. However, during deformation at elevated temperature (> 250°C), nonbasal slip systems are activated, thereby enabling the accommodation of large plastic deformations.^{1–5} Mg-Al-Zn (AZ)-based alloys are extensively used Mg-based alloys. AZ-based alloys exhibited nearly half the strength of mid-range Al-based alloys. However, AZ-based alloys are prone to abnormal grain growth and incipient melting during hot deformation processing, due to the low-melting-temperature Mg₁₇Al₁₂ phase.⁶ To impede abnormal grain growth, addition of trace amounts of rare-earth (RE) elements to Mg alloys can form a stable intermetallic phase that can stabilize

dynamically recrystallized grains and impede dislocation motion.^{7–9} However, the higher cost of RE elements limits the applications of such alloys.

Lightweight Mg-Sn alloys are promising structural materials that can be used in as-cast or wrought form. These alloys are also known to exhibit high thermal stability. The secondary phase Mg₂Sn in these alloys has a high melting temperature (770°C), which contributes to their thermal stability. Indeed, the thermal stability of Mg₂Sn phase is comparable to that of intermetallic compounds formed in Mg-RE alloys. Mahallawy et al.¹⁰ and Kim et al.⁸ demonstrated that Mg alloys are strengthened using intermetallic Mg₂Sn are superior to AZ-based alloys.^{8,10–12} The high thermal stability of these alloys enables their use in high-temperature applications. Chen et al.¹³ have also stated that minor alloying with Sn contributes to the formation of finely dispersed Mg₂Sn particles, thus leading to improved strength at ambient and elevated temperatures. However, the introduction of a higher concentration of Sn leads to coarsening of Mg₂Sn particles, thereby deteriorating the strength and ductility. Furthermore, Qi et al.¹² have reported that addition of Sn refines the

(Received November 20, 2020; accepted February 24, 2021;
published online March 24, 2021)

morphology of Mg-Zn by reducing the spacing for the eutectic phase along with the formation of a fine stable Mg_2Sn phase. Increasing the Sn content improves the strength with a concomitant deterioration of ductility. It was further suggested that the high strength is achieved because of precipitation strengthening by Mg_2Sn precipitates in the peak-aged condition. Cheng et al. and Shi et al. have reported that the growth of newly formed dynamically recrystallized (DRX) grains can also be controlled by fine Mg_2Sn precipitates through effective grain boundary pinning.^{14,15} For the present study, Al was selected as the third alloying element along with Sn. Addition of Al can improve the castability and solid-solution strengthening of Mg-Sn binary alloy at room temperature.^{16,17}

The overall aim of this work is to develop high-strength cost-effective Mg-based alloys. The Mg-Sn-Al alloy system has received attention as a promising candidate for materials in both as-cast and wrought processing conditions. In the present work, TA32 alloy was prepared by the squeeze casting (SC) technique. The SC ingot was homogenized at 300°C for 24 h (designated as H300), followed by hot rolling and annealing as one of the wrought processing techniques. The evolution of the microstructure, texture, and mechanical properties and their correlation is explored.

EXPERIMENTAL PROCEDURES

Materials

Commercial pure Mg (99.90 wt.%), Sn (99.85 wt.%), and Al (99.90 wt.%) were cut from a bulk ingot and weighed before being charged into a graphite crucible to be melted at 720°C in an electric resistance pit furnace under argon (Ar) atmosphere. The elemental composition was measured to be Mg-3Sn-2Al (wt.%). Squeeze casting (SC) was adopted because it is one of the better casting routes to obtain refined microstructure. During the squeeze casting, hot metal was poured into a preheated (200°C) cylindrical die ($\varnothing 75$ mm \times 75 mm) and pressure of 100 MPa was applied until complete solidification. The chemical composition of the alloy was determined by electron probe microanalysis (EPMA; JAXA 8530, JEOL) equipped with energy-dispersive spectrometry (EDS) and wavelength-dispersive spectrometry (WDS). The as-cast ingot was machined into plates with dimensions of 30 mm \times 30 mm \times 10 mm. The plates were homogenized at 300°C for 24 h, followed by hot rolling at 350°C with 90% reduction in thickness (10% thickness reduction per pass) (designated as HR). After hot rolling, the alloy sheet was annealed at 215°C for 30 min (designated as HRA).

Microstructural Analysis

Mg-Sn-Al samples for microscopic characterization were mechanically polished and prepared by

conventional metallographic methods. Optical microscopy (OM, inverted Axiovert MAT2000; CARL ZEISS), scanning electron microscopy (ESEM Quanta) equipped with EDS, and transmission electron microscopy (TEM, TM T20, Tecnai) were used to examine the microstructure. In addition, x-ray diffraction (PANalytical X'Pert PRO) was employed to analyze the phases present in the TA32 alloy.

X-ray measurements of the bulk texture were carried out on the mid-section of the rolled sheet. Textures were measured for HR and HRA samples using a Bruker D8 Discover x-ray texture goniometer with a Cu source ($\lambda = 1.54$ Å). The six pole figures (PFs) on the planes (10 $\bar{1}$ 0), (0002), (10 $\bar{1}$ 1), (10 $\bar{1}$ 2), (11 $\bar{2}$ 0) and (10 $\bar{1}$ 3) were measured. From the PF results, the orientation distribution functions (ODFs) were calculated using the MATLAB Mtex tool.

Tensile Tests

Tensile test specimens were machined from the rolled sheet in three orientations (i.e., 0°, 45°, and 90° to the rolling direction (RD)). Tensile specimens were prepared as per ASTM B-557 standard, and tensile tests were conducted on an Instron 5967 machine in 0° (RD), 45D (45° to the RD), and TD (90° to the RD) orientations at room temperature and constant strain rate of 1×10^{-3} s⁻¹.

RESULTS AND DISCUSSION

XRD and Microstructural Analysis

XRD Analysis

X-ray diffraction (XRD) analysis was conducted on the samples in both H300 and HR condition, and the patterns were recorded to determine the various phases present in the TA32 alloy. The XRD patterns for the H300 and HR conditions are shown in Fig. 1.

Both diffraction patterns revealed the presence of α -Mg and Mg_2Sn phases. The hot-rolled sample showed significant variation in the x-ray diffraction pattern, providing preliminary information about the crystallographic texture developed in the alloy. It was observed that α -Mg shows the highest peak intensity at the prismatic (10 $\bar{1}$ 0) plane for the H300 sample. However, for the HR sample, the maximum peak intensity for α -Mg was identified at the basal (0002) plane, indicating that the alloy was textured after hot processing.

As-Cast Microstructure

In the present investigation, TA32 alloy was produced by squeeze casting. Figure 1a shows optical micrographs of TA32 alloy in H300 condition. The microstructure consists of equiaxed grains with average size of 160 ± 37 μ m, as shown in the inset of Fig. 1a. Detailed microstructural characterization was carried out by SEM. Figure 1b shows

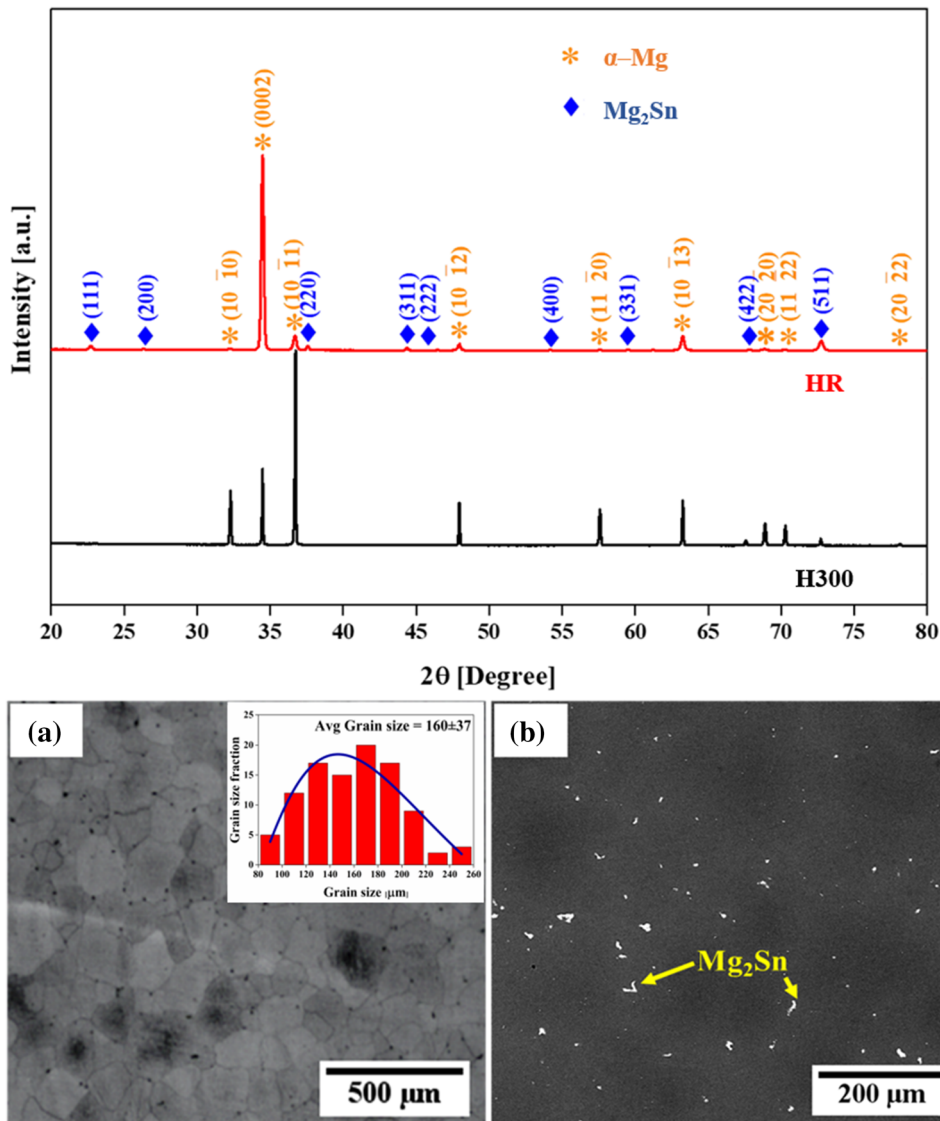


Fig. 1. XRD analysis of TA32 alloy in H300 and HR conditions: (a) optical and (b) SEM micrographs of H300.

SEM–BSE (*Z*-contrast) micrographs for TA32 alloy in H300 condition. It was observed that the second phase was present along the grain boundary. The phases of α -Mg (matrix) and second-phase Mg_2Sn particles are shown in Fig. 1b. The SEM–EDS analysis of α -Mg and Mg_2Sn phases also corroborates the XRD analysis (Fig. 1).

Hot-Rolled Microstructure

Figure 2 shows micrographs of TA32 alloy after hot deformation. It is also observed that Fig. 2a shows numerous twins in the HR micrographs. Figure 2b shows SEM–BSE (*Z*-contrast mode) HR micrographs. Hot rolling deformed the homogenized microstructure and changed the aspect ratio of the grains. Meanwhile, the Mg_2Sn phase that was present along the grain boundary fragmented and aligned along the rolling direction, as shown in

Fig. 2b. The morphology of the Mg_2Sn particles was observed to be globular after hot rolling (see higher magnification in Fig. 2b). Moreover, the Mg_2Sn particles were fine and well distributed in the HR condition. Grain refinement occurred during hot rolling, and the grain size was calculated to be $13 \pm 3 \mu\text{m}$. Figure 2c and d shows bright-field TEM images and a selected-area diffraction (SAD) pattern obtained from the area of matrix and fine particles of Mg_2Sn phase in the TA32 alloy.

Figure 3a, b, c, and d shows optical micrographs of TA32 alloy in HR and HRA conditions at different magnifications, including grain size distribution plots with twinning activity. The grain size was calculated to be $13 \pm 3 \mu\text{m}$ and $18 \pm 3 \mu\text{m}$ for the HR and HRA condition, respectively (Fig. 3a and c).

Mg_2Sn particles play a part in the microstructural evolution of Mg–Sn-based alloys. The H300 microstructure (Fig. 1b) consists of relatively coarse

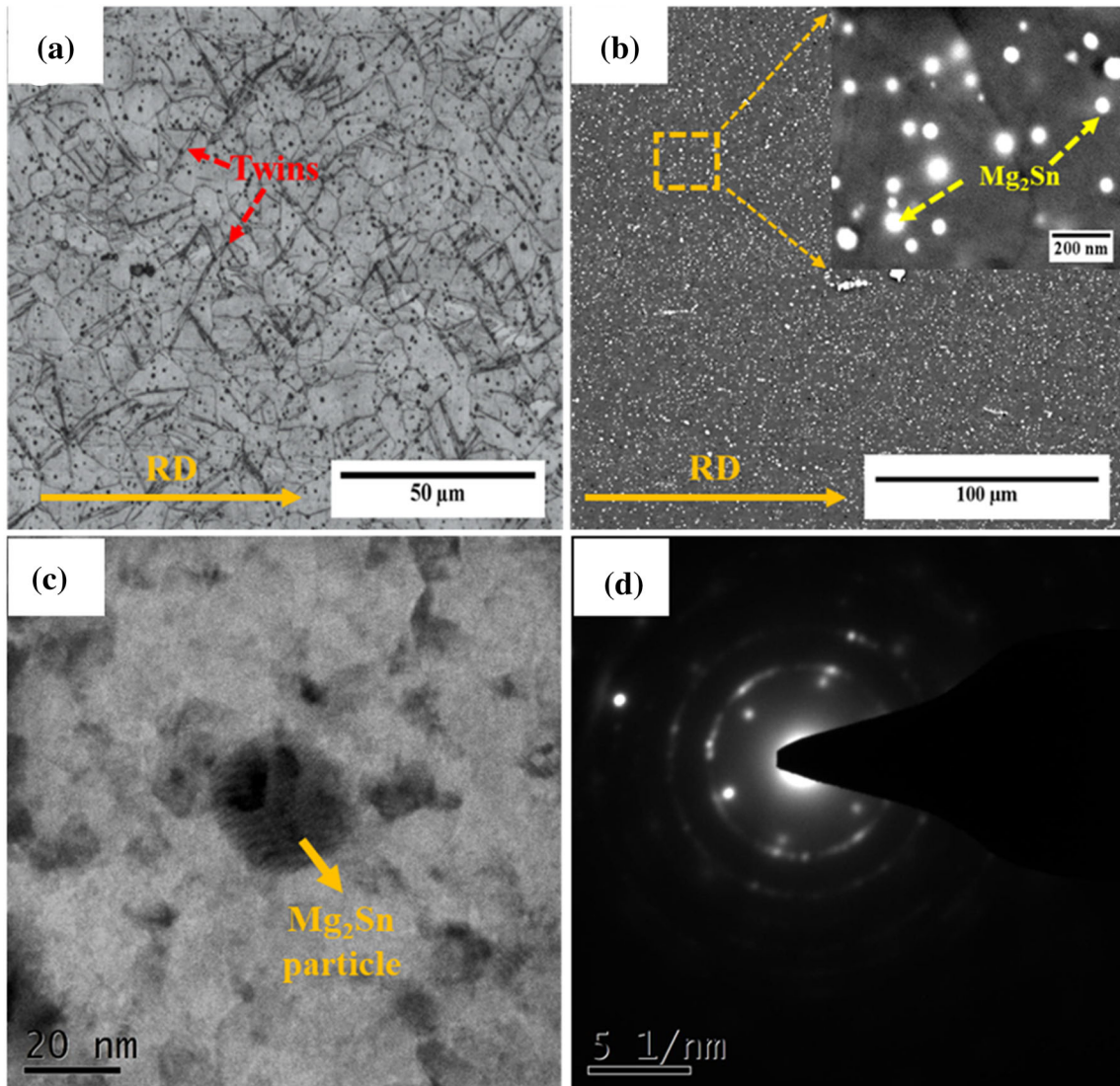


Fig. 2. TA32 alloy in HR condition: (a) optical, and (b) SEM–BSE micrographs showing fine Mg_2Sn particle distribution, (c, d) bright-field TEM image of a fine particle with SAD pattern.

Mg_2Sn particles, accumulated along the grain boundaries.

The Mg–Sn alloy phase diagram shows that the maximum solid solubility of Sn in Mg is 14.48 wt.% at 561°C (eutectic temperature) while its solubility reduces to 0.45 wt.% at 200°C and is negligible at ambient temperature.¹⁸ During the process of squeeze casting the host matrix, α -Mg acquires solutes of Sn and Al. The excess Sn atoms come out by minimization of energy of the supersaturated α -Mg (matrix) during homogenization at 300°C in the form of fine Mg_2Sn particles, which further increases the volume fraction. The microstructure of samples in HR condition is shown in Fig. 2, revealing refinement in the homogenized microstructural features. Hot rolling led to a reduction in the grain size (13 μm) and fragmentation of the coarse Mg_2Sn particles and are uniformly distributed as finer Mg_2Sn particles. In the strained

regions, the distribution of the Mg_2Sn particles was observed to be along the RD. The growth of dynamic recrystallization (DRX) grains can be suppressed by the effective grain-boundary pinning effect of the fine Mg_2Sn particles.^{14,19} Therefore, the fine Mg_2Sn particles and dynamic recrystallization substantially provide a refinement effect in the microstructure after hot rolling. In contrast, it was observed that, in the HRA sample, the microstructural features remained the same. However, the HRA samples showed a minimal increment in grain size.

Evolution of Texture Due to Deformation

Figure 4 illustrates the basal (0002) and prismatic (10 $\bar{1}$ 0) and (11 $\bar{2}$ 0) pole figures (PFs) for the HR and HRA conditions. It was observed that the basal texture (maximum intensity 8.6) (Fig. 4a) developed after the hot rolling process. However, for the HRA

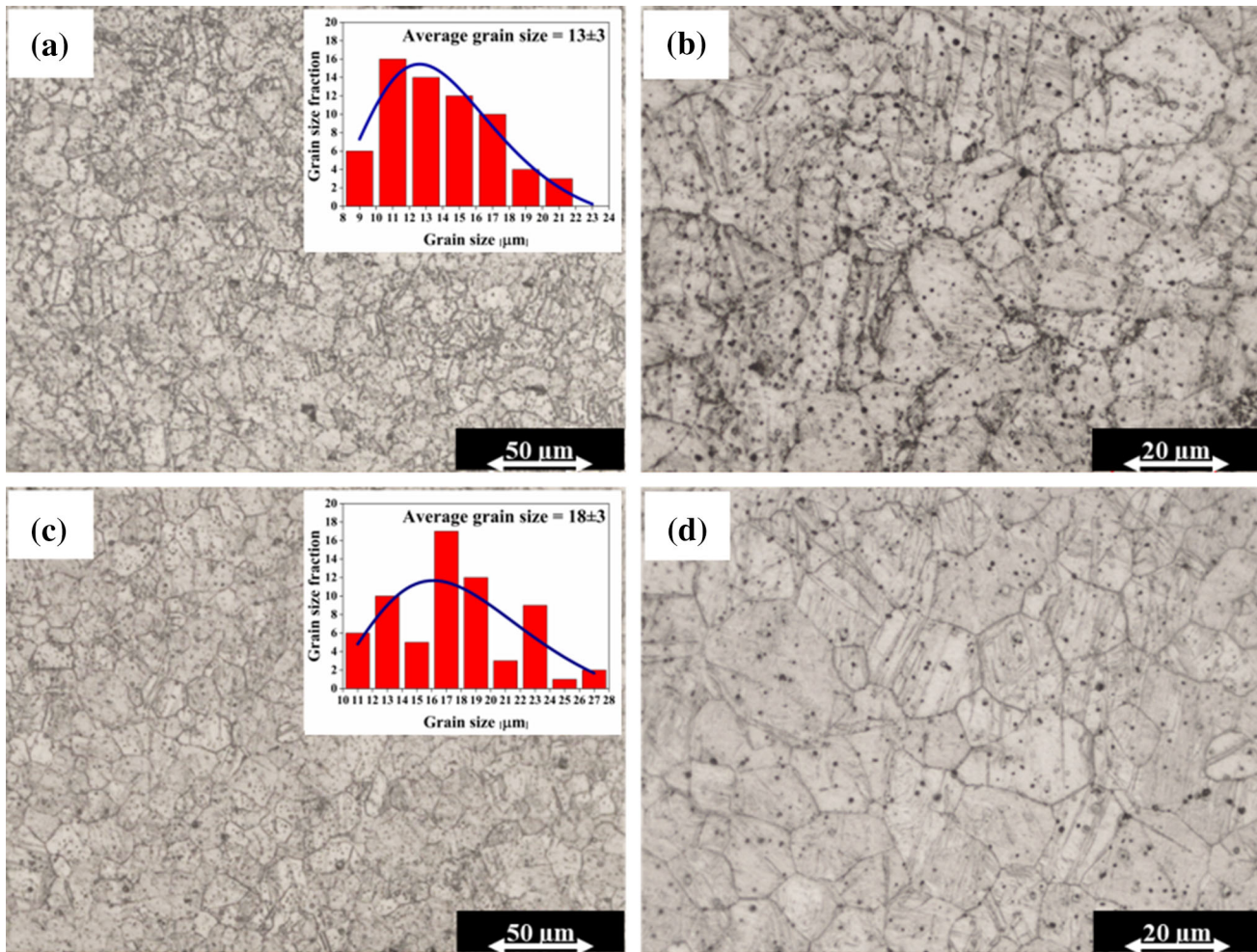


Fig. 3. Microstructure (OM) of TA32 alloy in (a, b) HR, and (c, d) HRA condition at different magnifications.

sample, the basal pole intensity (maximum intensity 6.4) is seen to decrease and spread towards the RD from ND plane, as shown in Fig. 4b.

Figure 4c and d shows the $\varphi_2 = 0^\circ$ and 30° sections of the orientation distribution function (ODFs) for the HR and HRA condition. Continuous basal fiber is seen in the ODF sections. The maximum intensity was recorded to be 8.9 for the HR sample. However, the maximum intensity was reduced to 6.4 for the HRA sample.

Crystallographic orientation plays a major part during the hot processing of nonisotropic material. In the case of Mg (with HCP crystal structure), the slip systems are basal slip system $\{0001\}\langle 11\bar{2}0 \rangle$, prismatic slip system $\{10\bar{1}0\}\langle 11\bar{2}0 \rangle$, pyramidal I slip systems $\{10\bar{1}1\}\langle 11\bar{2}0 \rangle$ and $\{10\bar{1}2\}\langle 11\bar{2}0 \rangle$, and pyramidal II slip system $\{11\bar{2}2\}\langle 11\bar{2}3 \rangle$. Each slip system is activated when the critical resolved shear stress (CRSS) exceeds the corresponding threshold stress value. The basal slip system plays a dominant role during room-temperature deformation due to its lowest CRSS value. When the deformation temperature exceeds 250°C , the nonbasal

(prismatic) slip system gets activated. At deformation temperatures above 350°C , the pyramidal slip system also contributes significantly to deformation, which leads to higher formability.^{4,5}

The basal (0002) texture was observed only after hot rolling, which is similar to the conventional rolling texture in Mg and its alloys.²⁰ In the HRA condition, the basal (0002) pole intensity was reduced to 6.4 and spread from ND to RD (Fig. 4b). Koundinya et al. and Wang et al. have also reported that, in Mg-Sn-based alloys, the spreading of the basal pole intensity is due to multiple slip system activity, caused by the presence of Al atoms in the solid solution.^{20,21}

Tensile Behavior in HR and HRA Conditions

The tensile properties of the H300 sample were found to be 0.2% PS of 81 MPa, UTS of 229 MPa, and ductility of 12%. To evaluate the anisotropic tensile behavior of TA32 alloy, tensile tests were performed in RD, 45D, and TD orientations. Figure 5a shows true stress–true strain plots for the TA32 alloy in HR condition. It was observed that the

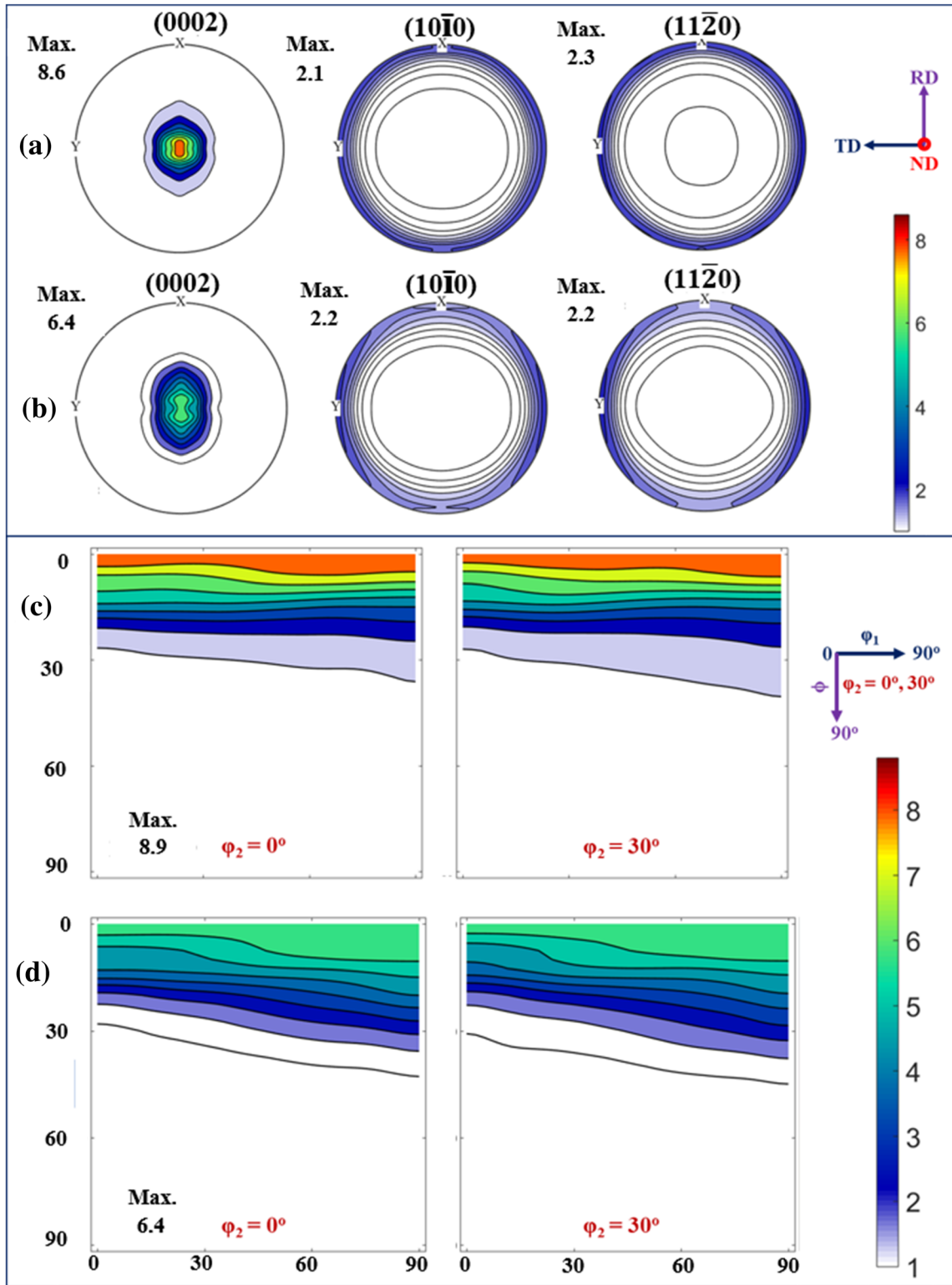


Fig. 4. (0002) , $(10\bar{1}0)$, and $(11\bar{2}0)$ PFs of TA32 alloy in (a) HR and (b) HRA condition; ODF sections ($\phi_2 = 0^\circ$ and 30°) of TA32 alloy in (c) HR and (d) HRA conditions.

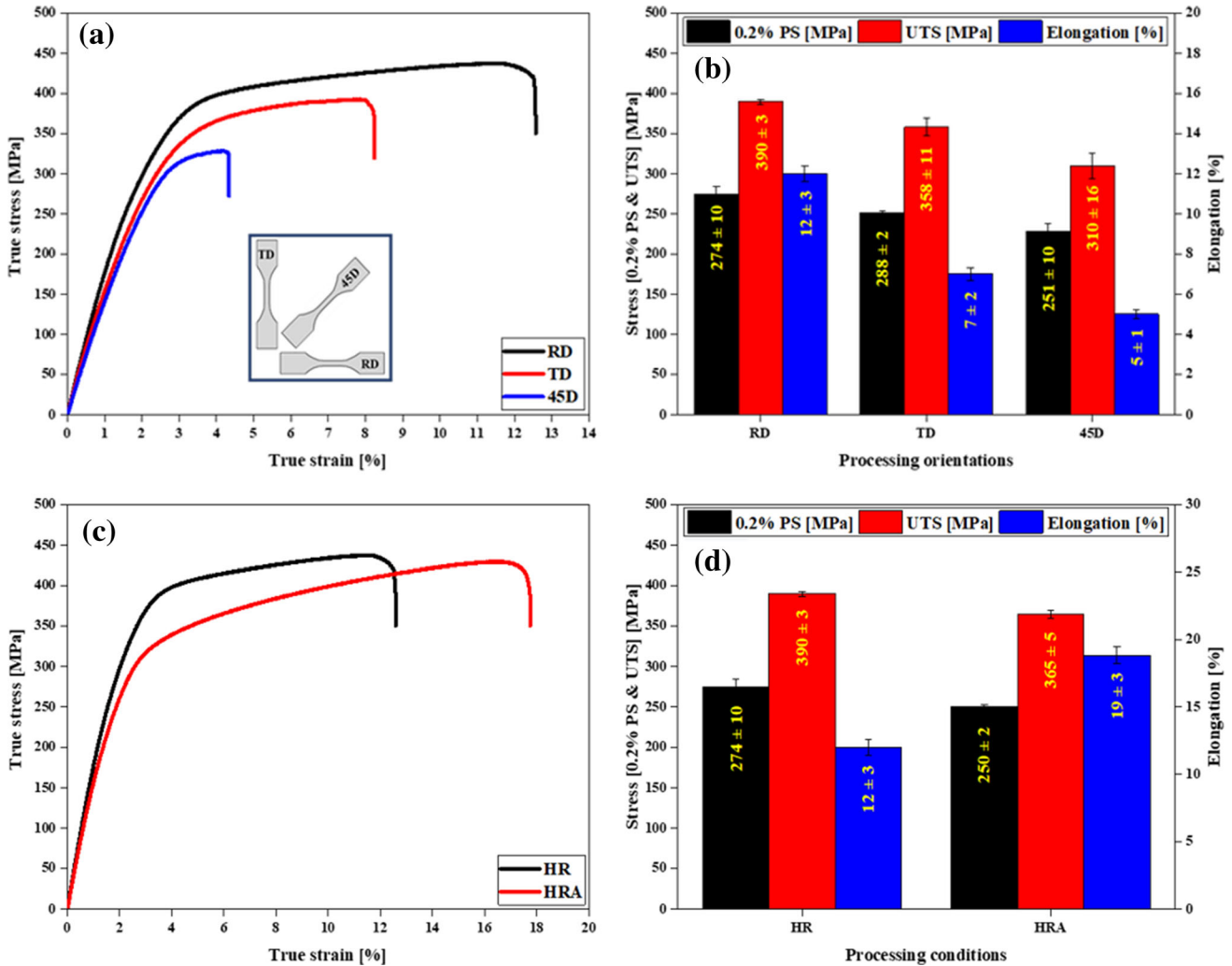


Fig. 5. Tensile properties of TA32 alloy in HR condition: (a) true stress–strain curves, and (b) tensile properties in three orientations; TA32 alloy in HR and HRA conditions: (c) Tensile curves, and (d) tensile properties in RD orientation.

RD showed the highest tensile strength and ductility. However, 45D reported the minimum ductility with the lowest strength. TD orientation exhibited intermediate strength and ductility. The tensile properties for TA32 alloy in HR conditions are shown in Fig. 5b.

The tensile properties of TA32 alloy depend on the orientations of the tensile test directions, i.e., RD, 45D, or TD. It has been observed that TA32 alloy exhibits anisotropic tensile behavior. It is well known that the yield stress of polycrystalline materials depends on the CRSS and orientation. The 45D specimen exhibited the lowest %El as compared with the RD and TD orientations. However, RD samples showed the optimum combination of strength and ductility.

To achieve the optimum combination of tensile properties, i.e., strength and ductility, HR samples were annealed at 215°C. Figure 5c shows the true stress–true strain plots of the TA32 alloy in HR and HRA conditions. The highest ductility (19%) was achieved in the HRA sample with the optimum

strength (0.2% PS of 250 MPa, UTS of 365 MPa). The tensile properties for the HR and HRA conditions are summarized in Fig. 5d.

The strength of the HR sample was significantly improved with a marginal improvement in ductility as compared with the H300 sample. Thus, excellent strength with reasonable ductility was achieved for the HR sheet (0.2% PS of 274 MPa, UTS of 390 MPa, and ductility of 12%). The ductility was further increased (19%) albeit with a moderate reduction in strength for the HRA sample (0.2% PS of 250 MPa and UTS of 305 MPa). The HRA sample showed a slight increase in grain size. The HRA sample was found to exhibit the best combination of strength and ductility.

It is well known that larger grains contain more twins because they have larger grain boundary areas and larger grain volumes, and the deformation process of large grains is chiefly mediated by deformation twinning. The rapid decrease in hardening rate can be attributed to twinning, while the gentle decline is ascribed to slip, which is consistent

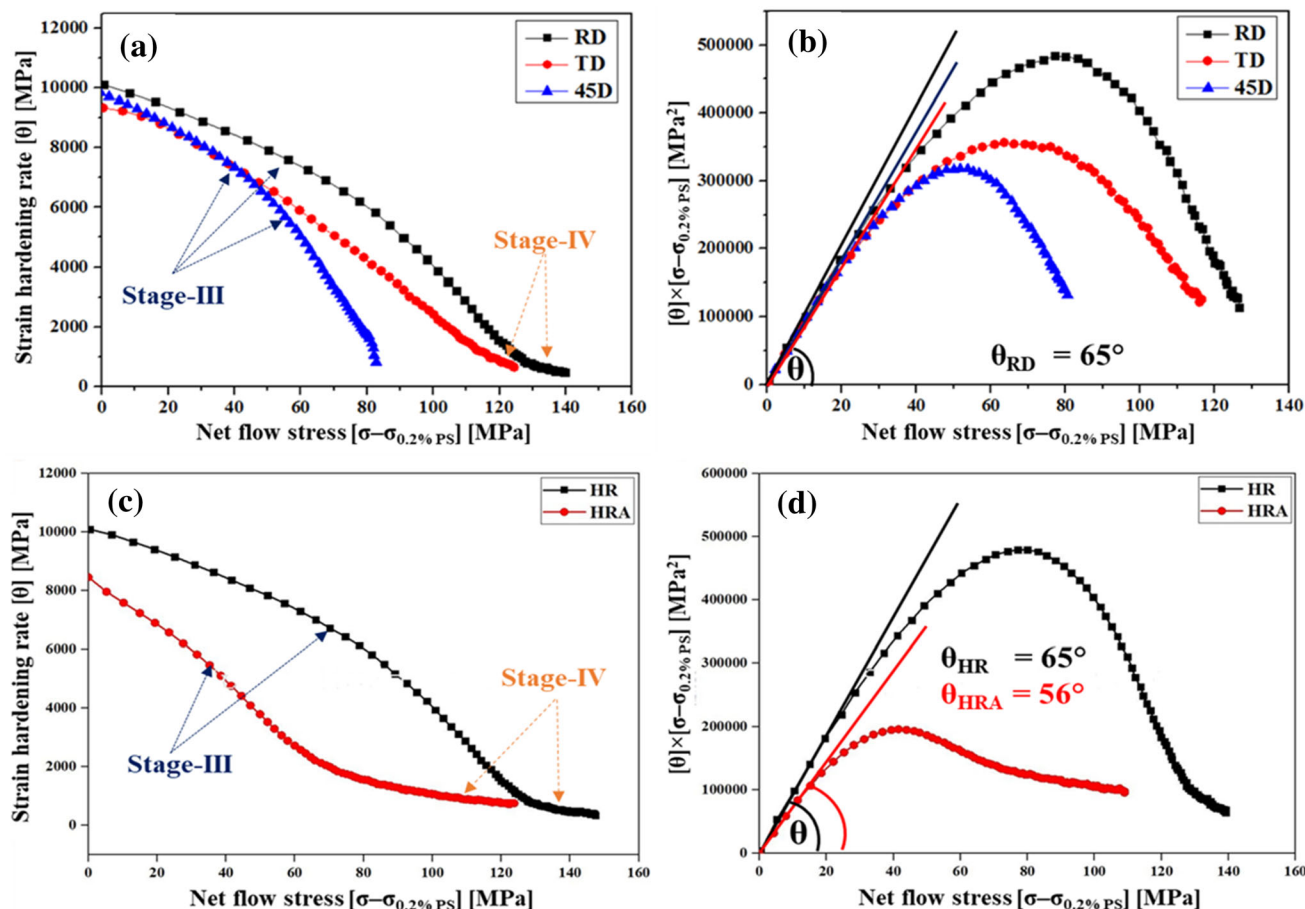


Fig. 6. Anisotropic hardening curves of TA32 alloy in HR condition: (a) KM I and (b) KM II plots; TA32 alloy in HR and HRA conditions: (c) KM-I and (d) KM-II plots.

with the results obtained by Koike.²² Dislocation accumulation and multiplication at twin boundaries lead to strengthening by strain hardening. During annealing at 215°C, static recrystallization led to an increase in ductility while maintaining the strength. Strong dislocation accumulation is found around the nanosized Mg₂Sn particles, which contribute to the tensile strength. Furthermore, the fragmentation and precipitation of the fine Mg₂Sn particles suppress DRX grain growth and impede dislocation motion.²³

The strain hardening rate (θ) is defined as the instantaneous change in stress for an instantaneous change of strain, which can be expressed mathematically by the following equation:^{24,25}

$$\theta = \frac{\partial \sigma}{\partial \varepsilon} \quad (1)$$

where σ and ε denote the stress and strain, respectively. This equation has been proposed by Kocks and Mecking and presented as a Kocks–Mecking (KM) plot.^{26,27} The KM plots for the three orientations are shown in Fig. 6a and b. The hardening rate linearly decreased up to net flow stress of 50 MPa. A marginal change in strain hardening can be

observed between RD and TD samples, which corresponds to stage III hardening. A downward trend is observed in the hardening rate between 80 MPa and 100 MPa. Eventually, both RD and TD samples show plateauing at higher net flow stress indicating saturation, which is a typical stage IV hardening behavior. For all three orientations, stage III and stage IV hardening were observed. It can also be noted that the 45D-oriented sample exhibited a quick drop in hardening in the stress range from 60 MPa to 80 MPa.

The plots in Fig. 6b clearly illustrate a variation in stress from the $\theta \times (\sigma - \sigma_{0.2\%PS})$ versus net flow stress, and the tensile curves for the TA32 alloy in the three orientations (i.e., RD, 45D, and TD). It can be seen that the initial part of the hardening curves fit a linear curve with slope θ_h . The hardening curve of RD-oriented sample was linear, up to 65 MPa to 70 MPa, unlike the other two samples. The initial hardening behavior of the TA32 alloy could be described by homogeneous straight lines. Afrin et al.,²⁸ Kocks et al.,²⁶ and Wu et al.²⁹ reported similar results for face-centered cubic (FCC) polycrystals. The downward trend of the curves at higher stresses can be attributed to the onset of

dynamic recovery, which corresponds to the declining slope of stress–strain curves. Therefore, a relatively faster onset of dynamic recovery is seen in 45D, followed by TD, and finally the RD orientation samples, which is due to increased cross-slip in processed TA32 alloy.

The strain hardening ability of TA32 alloy is characterized using the KM plot for the HR and HRA conditions in Fig. 6c. A rapid decrease in hardening rate can be observed at the initial deformation stage, then retardation at a later stage. The hardening rate is seen to be linearly decreasing with increasing net flow stress, which corresponds to stage III hardening. For higher net flow stress, the hardening rate becomes saturated, which is characteristic of stage IV hardening. For the HR sample, the highest strain hardening rate ($\theta_{II} = 10,000$ MPa) is observed followed by stage III and stage IV hardening. However, for the HRA condition, at the beginning of the hardening, the alloy shows early stage III hardening. Thereafter, stage IV hardening dominates. Figure 6d shows the $\theta \times (\sigma - \sigma_{0.2\%PS})$ versus net flow stress curves for TA32 alloy in HR and HRA condition. The downward curvature of the hardening curves at high net flow stresses indicates the onset of dynamic recovery. Early onset of dynamic recovery occurs in the HRA compared with HR condition.

Strain field interactions and dislocations play a major role in the strain hardening of material after yielding. A strengthening role of the dislocation density was proposed by Taylor, which can be expressed by the following mathematical equation:^{29–31}

$$\sigma_d = M\eta Gb\sqrt{\rho} \quad (2)$$

where M is the Taylor factor, η is a constant, G (GPa) is the shear modulus, b (Å) is the Burgers vector, and ρ (cm^{-3}) is the dislocation density. Kocks and Mecking showed in their seminal paper that the stress applied to deform a material is proportional to the dislocation density inside the material, which is shown in a high and nearly constant strain hardening rate (i.e., stage II).²⁶ The softening effect occurs due to dislocation annihilation by dynamic recovery (stage III), which is affected by the applied stress and temperature.³² In TA32 alloy, the element Al strengthens by solid-solution strengthening, which is mainly due to the large difference in atomic radius between Mg ($r_{\text{Mg}} = 1.60$ Å) and Al ($r_{\text{Al}} = 1.43$ Å), whereas in the case of Sn ($r_{\text{Sn}} = 1.58$ Å), this effect is negligible. The main reason for adding Al and Sn is to reduce the stacking fault energy for different slip systems (i.e., $\{10\bar{1}1\}\langle 11\bar{2}0\rangle$ and $\{11\bar{2}2\}\langle 11\bar{2}3\rangle$), which would promote initiation of nonbasal dislocation slip.

The tensile properties of TA32 alloy are dependent on the grain size of the matrix, the solid solubility of Al and Sn, the size and volume fraction of Mg_2Sn particles, and the crystallographic

texture. The grain boundary (GB) strengthening can be expressed as follows:^{7,33,34}

$$\sigma_y = \sigma_o + \frac{k}{\sqrt{d}} \quad (3)$$

where $\sigma_o = 21$ MPa and $k = 300$ MPa $\sqrt{\mu\text{m}}$, whereas solid-solution (SS) strengthening is described by the equations^{34,35}

$$\Delta\sigma_{\text{SS}} = \left[\sum_i \left\{ (K_i)^{\frac{1}{n}} \times (C_i) \right\} \right]^n \quad (4)$$

$$\Delta\sigma_{\text{SS}} = \left[\left\{ (K_{\text{Sn}})^{\frac{1}{n}} \times (C_{\text{Sn}}) \right\} + \left\{ (K_{\text{Al}})^{\frac{1}{n}} \times (C_{\text{Al}}) \right\} \right]^n \quad (5)$$

where $n = \left[\frac{2}{3}\right]$, $K_{\text{Sn}} = 389$ MPa $\left[\left(\text{at.}\% \right)^{\frac{2}{3}}\right]$, $K_{\text{Al}} = 196$ MPa $\left[\left(\text{at.}\% \right)^{\frac{2}{3}}\right]$, $C_{\text{Sn}} = 0.7$ at.%, and $C_{\text{Al}} = 2.7$ at.%. .

The strengthening contribution of GB and SS were calculated to be 44.72 MPa and 25.12 MPa for the H300 condition. Similarly, these strengthening contributions were evaluated to be 104.21 MPa and 25.37 MPa for HR, and 91.72 Pa and 26.07 MPa for HRA. The tensile properties of the H300 sample were the lowest due to the relatively coarser Mg_2Sn particles present in the microstructure. The presence of the coarse Mg_2Sn particles along the grain boundary causes premature failure of the alloy. The improvement in strength after HR can mainly be ascribed to microstructural refinement and solid-solution strengthening of Al and Sn solutes in the matrix. During hot rolling, stable Mg_2Sn precipitates are formed and evenly dispersed in the matrix as well as at grain boundaries. In addition, a higher volume of fine Mg_2Sn particles and strain gradient inside the material lead to the strength improvement. Furthermore, Peng et al. stated that extensive formation of intersectional twins is solely responsible for the higher strain hardening rate.⁹ The fundamental mechanism of strain hardening ability occurs via deformation twins. This plays a vital role in hindering non-coplanar slip by dislocation pile-up and storage at twin-matrix boundaries.

Interestingly, TA32 alloy in HR condition exhibits high tensile strength with 0.2% PS of 274 MPa and UTS of 390 MPa, as well as reasonable ductility of 12% in the RD orientation, which is superior to the values for conventional AZ31 alloy with 0.2% PS of 242 MPa, UTS of 305 MPa, and ductility of 14%.⁶ (Fig. 7a and b).

Fractography in HR and HRA Conditions

Figure 8a, b, and c shows the fractography results for the tensile samples in the three orientations (i.e., RD, 45D, and TD) for TA32 alloy in HR condition. Figure 8d, e, and f shows the Mg_2Sn particles on the fracture surface. The main fracture modes in the Mg-based alloys are intergranular and quasi-

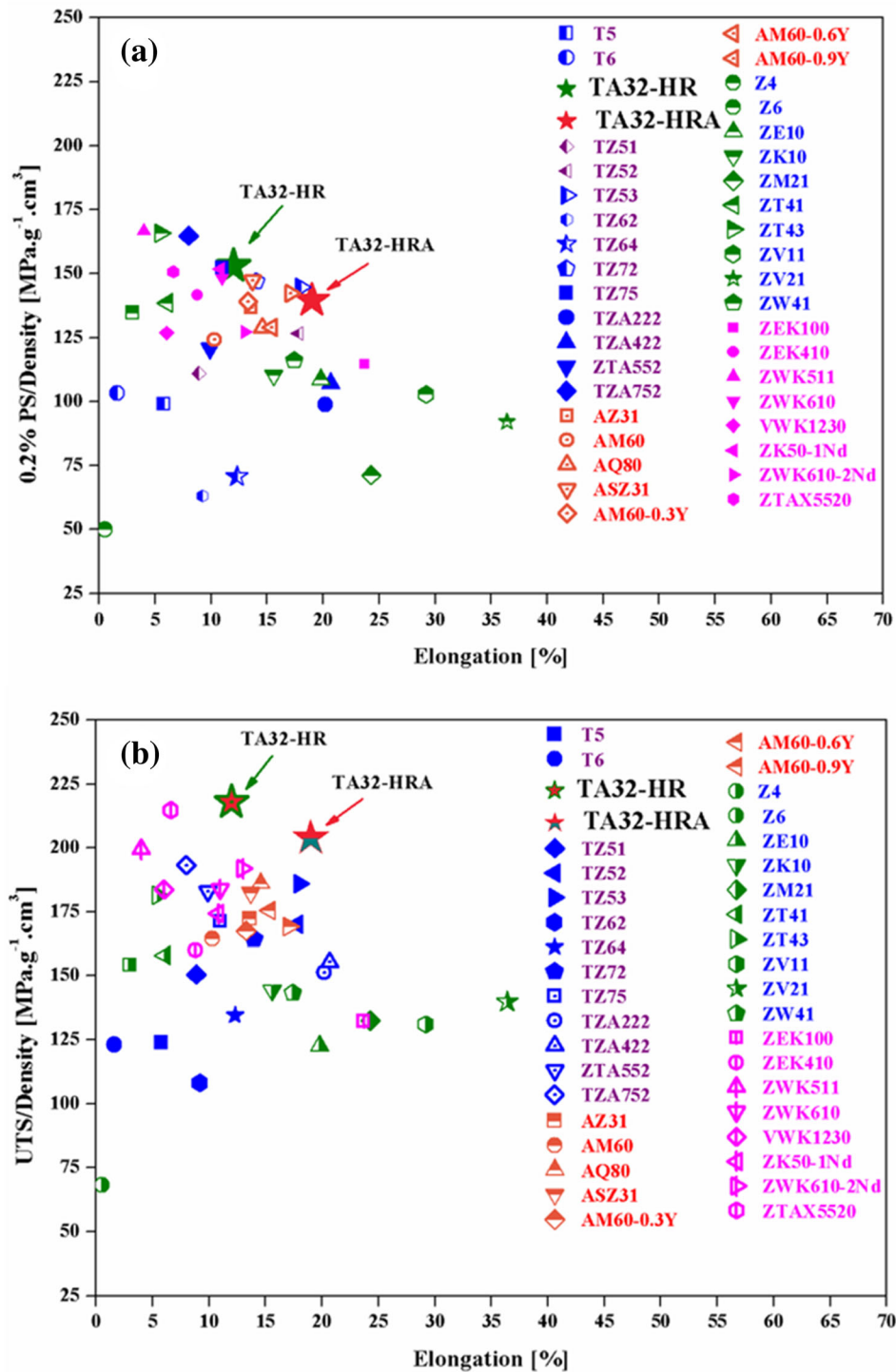


Fig. 7. Comparison of (a) specific yield strength (0.2% PS/density), and (b) specific ultimate tensile strength (UTS/density) of TA32 alloy with some of the experimental and commercial wrought Mg-Sn, Mg-Al, Mg-Zn, and Mg-RE-based alloys.^{6,14,36-43}

cleavage. The dimples were distributed throughout the fracture surface in all three orientations.

Figure 8g, h, and i illustrates the fractography results of TA32 alloy in the HRA condition. The fracture surface shows large volume fraction of fine dimples and cleavage-type facets that lead to quasi-cleavage fracture. The fractography shows that the

fine Mg₂Sn particles were uniformly distributed in the matrix; the effect is observed in the form of fine dimples. The Mg₂Sn particles were also distributed along the grain boundaries, which led to initiation and propagation of cracks along the grain boundaries. This resulted in intergranular and quasi-cleavage-type fracture.

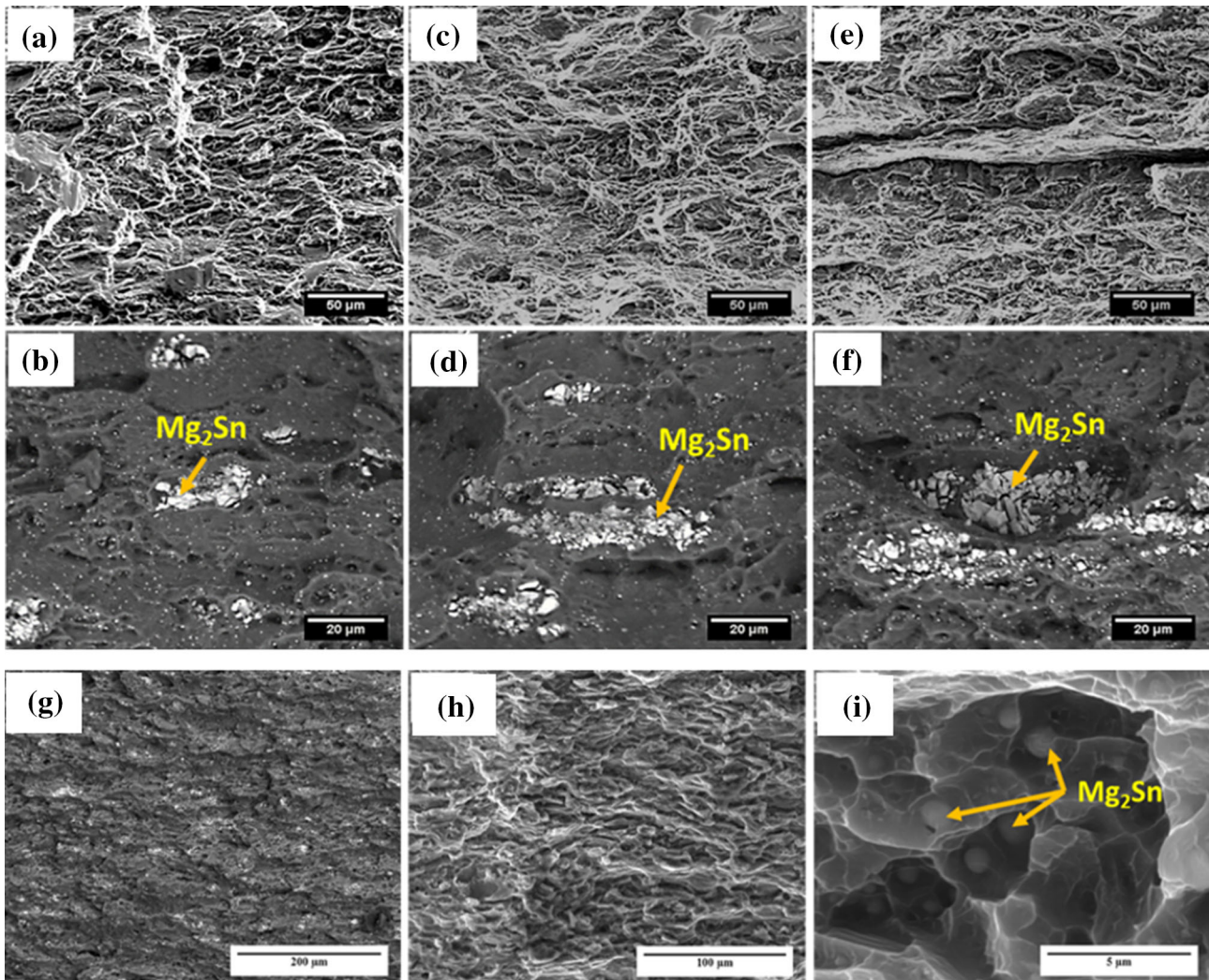


Fig. 8. Fractography of TA32 alloy in HR condition: (a, b) RD, (c, d) 45D, and (e, f) TD orientations; HRA condition at different magnifications (g–i).

CONCLUSION

TA32 alloy was prepared and processed by squeeze casting. The samples were homogenized at 300°C for 24 h (H300) followed by hot rolling and annealing. The microstructure was characterized, and the tensile properties were compared with those of commercial AZ31 alloy and other experimental Mg-based alloys. The following major conclusions can be drawn from the results:

- (1) Hot rolling at 350°C refined the microstructural features compared with H300.
- (2) The uniform distribution of thermally stable fine Mg_2Sn particles in the alloy is responsible for suppressing the growth of DRX grains during hot rolling.
- (3) HR samples exhibited very high strength with 0.2% PS of 274 MPa and UTS of 390 MPa as well as reasonable ductility (12%) with minimum tensile anisotropy.

- (4) HRA samples exhibited good strength and higher ductility (0.2% PS of 250 MPa, UTS of 365 MPa, and ductility of 19%).
- (5) The excellent strength of the alloy can be attributed to the synergistic effect of grain refinement, solid-solution strengthening by Al and Sn atoms, and the uniform distribution of fine Mg_2Sn particles.
- (6) The reported tensile properties for TA32 alloy are better than those of most commercially available and experimental Mg-based alloys.

ACKNOWLEDGEMENTS

The authors gratefully acknowledged Prof. Saityam Suwas, Chairperson of the Department of Materials Engineering, Indian Institute of Science (IISc), Bangalore, India for allowing us to use characterization facilities available in the department.

CONFLICT OF INTEREST

The authors declare that they have no known competing financial interests or personal relationships that could have appeared to influence the work reported in this paper.

REFERENCES

- E. Aghion, B. Bronfin, and D. Eliezer, *J. Mater. Process. Technol.* 117, 381. [https://doi.org/10.1016/S0924-0136\(01\)00779-8](https://doi.org/10.1016/S0924-0136(01)00779-8) (2001).
- B. Mordike, and T. Ebert, B. Mordike, and T. Ebert, *Mater. Sci. Eng. A* 302, 37. [https://doi.org/10.1016/S0921-5093\(00\)01351-4.N](https://doi.org/10.1016/S0921-5093(00)01351-4.N) (2001).
- K. Hono, C.L. Mendis, T.T. Sasaki, and K. Oh-Ishi, *Scr. Mater.* 63, 710. <https://doi.org/10.1016/j.scriptamat.2010.01.038> (2010).
- C. Bettles and M. Barnett, *Advances in Wrought Magnesium Alloys: Fundamentals of Processing, Properties and Applications*, 2012. ISBN 978-1-84569-968-0.
- I. Polmear, *Light Alloys: Tradit. Alloys Nanocryst.* <https://doi.org/10.1017/S000192400008670X> (2005).
- L. Zheng, H. Nie, W. Zhang, W. Liang, and Y. Wang, *Mater. Sci. Eng. A* 722, 58. <https://doi.org/10.1016/j.msea.2017.12.048> (2018).
- L. Gao, R.S. Chen, and E.H. Han, *J. Alloys Compd.* 481, 379. <https://doi.org/10.1016/j.jallcom.2008.04.049> (2009).
- H.K. Lim, D.H. Kim, J.Y. Lee, W.T. Kim, and D.H. Kim, *J. Alloys Compd.* 468, 308. <https://doi.org/10.1016/j.jallcom.2007.12.098> (2009).
- Q. Peng, X. Hou, L. Wang, Y. Wu, Z. Cao, and L. Wang, *Mater. Des.* 30, 292. <https://doi.org/10.1016/j.matdes.2008.04.069> (2009).
- N.E. Mahallawy, A.A. Diaa, M. Akdesir, and H. Palkowski, *Mater. Sci. Eng. A* 680, 47. <https://doi.org/10.1016/j.msea.2016.10.075> (2017).
- D. Luo, N. Xia, H.-Y. Wang, L. Chen, J.-G. Wang, and Q.-C. Jiang, *Mater. Sci. Technol.* 30, 1305. <https://doi.org/10.1179/1743284714Y.0000000565> (2014).
- F. Qi, D. Zhang, X. Zhang, and X. Xu, *J. Alloys Compd.* 585, 656. <https://doi.org/10.1016/J.JALLCOM.2013.09.156> (2014).
- J. Chen, Z. Chen, H. Yan, F. Zhang, and K. Liao, *J. Alloys Compd.* 461, 209. <https://doi.org/10.1016/j.jallcom.2007.07.066> (2008).
- Z.-Z. Shi, J.-Y. Xu, J. Yu, and X.-F. Liu, *Mater. Sci. Eng. A* 712, 65. <https://doi.org/10.1016/j.msea.2017.11.094> (2018).
- W.L. Cheng, S.S. Park, B.S. You, and B.H. Koo, *Mater. Sci. Eng. A* 527, 4650. <https://doi.org/10.1016/j.msea.2010.03.031> (2010).
- Y. Chen, L. Jin, Y. Song, H. Liu, and R. Ye, *Mater. Sci. Eng. A* 612, 96. <https://doi.org/10.1016/j.msea.2014.06.022> (2014).
- D.H. Kim, Y.K. Kim, S.W. Sohn, D.H. Kim, and W.T. Kim, *J. Alloys Compd.* 549, 46. <https://doi.org/10.1016/j.jallcom.2012.09.050> (2013).
- ASM International, *ASM Handbook, Volume 3, Alloy Phase Diagrams*, vol. 7, 2004. <https://doi.org/10.1007/BF02869318>.
- W.N. Tang, S.S. Park, and B.S. You, *Mater. Des.* 32, 3537. <https://doi.org/10.1016/J.MATDES.2011.02.012> (2011).
- Y.N. Wang, and J.C. Huang, *Mater. Chem. Phys.* 81, 11. (2003).
- N. Koundinya, L. Raman, N. Chawake, and R.S. Kottada, *Materialia* 3, 274. <https://doi.org/10.1016/j.mtla.2018.09.001> (2018).
- J. Koike, *Metall. Mater. Trans. A* 36A, 1689. <https://doi.org/10.1007/s11661-005-0032-4> (2005).
- J. Jiang, G. Bi, G. Wang, Q. Jiang, J. Lian, and Z. Jiang, *J. Magn. Alloys* 2, 116. <https://doi.org/10.1016/J.JMA.2014.05.004> (2014).
- H.-Y. Wu, and F.-Z. Lin, *Mater. Sci. Eng. A* 527, 1194. <https://doi.org/10.1016/J.MSEA.2009.09.049> (2010).
- C. Zhao, X. Chen, F. Pan, S. Gao, D. Zhao, and X. Liu, *Mater. Sci. Eng. A* 713, 244–252. <https://doi.org/10.1016/J.MSEA.2017.12.074> (2018).
- U.F. Kocks, and H. Mecking, *Prog. Mater. Sci.* [https://doi.org/10.1016/S0079-6425\(02\)00003-8](https://doi.org/10.1016/S0079-6425(02)00003-8) (2003).
- Y. Zou, L. Zhang, Y. Li, H. Wang, J. Liu, P.K. Liaw, H. Bei, and Z. Zhang, *J. Alloys Compd.* 735, 2625. <https://doi.org/10.1016/j.jallcom.2017.12.025> (2018).
- N. Afrin, D.L. Chen, X. Cao, and M. Jahazi, *Scr. Mater.* 57, 1004. <https://doi.org/10.1016/j.scriptamat.2007.08.001> (2007).
- H.Y. Wu, J.C. Yan, H.H. Tsai, C.H. Chiu, G.Z. Zhou, and C.F. Lin, *Mater. Sci. Eng. A* 527, 7197. <https://doi.org/10.1016/j.msea.2010.08.019> (2010).
- C.H. Cáceres, and A.H. Blake, *Mater. Sci. Eng. A* 462, 193. <https://doi.org/10.1016/j.msea.2005.12.113> (2007).
- A.D. Rollett, and U.F. Kocks, *Solid State Phenom.* 35–36, 1. <https://doi.org/10.4028/www.scientific.net/SSP.35-36.1> (1993).
- E.I. Poliak, and J.J. Jonas, *Acta Mater.* 44, 127. [https://doi.org/10.1016/1359-6454\(95\)00146-7](https://doi.org/10.1016/1359-6454(95)00146-7) (1996).
- W.L. Cheng, Q.W. Tian, H. Yu, H. Zhang, and B.S. You, *J. Magn. Alloys* 2, 299–304. <https://doi.org/10.1016/j.jma.2014.11.003> (2014).
- G. Hu, D. Zhang, T. Tang, X. Shen, L. Jiang, J. Xu, and F. Pan, *Mater. Sci. Eng. A* 634, 5. <https://doi.org/10.1016/j.msea.2015.03.040> (2015).
- L. Gao, R.S. Chen, and E.H. Han, *J. Alloys Compd.* 472, 234. <https://doi.org/10.1016/j.jallcom.2009.02.131> (2009).
- J. Bohlen, M.R. Nürnberg, J.W. Senn, D. Letzig, and S.R. Agnew, *Acta Mater.* 55, 2101. <https://doi.org/10.1016/J.AC.TAMAT.2006.11.013> (2007).
- Y. Chen, H. Liu, G.T. Gao, D. Fang, Y. Wang, L. Jin, and Y. Jiang, *Key Eng. Mater.* 727, 196. <https://doi.org/10.4028/www.scientific.net/KEM.727.196> (2017).
- N.E. Mahallawy, A.A. Diaa, M. Akdesir, and H. Palkowski, *Materwiss. Werksttech.* 47, 37. <https://doi.org/10.1002/mawe.201500468> (2016).
- Y.K. Kim, S.W. Sohn, D.H. Kim, W.T. Kim, and D.H. Kim, *J. Alloys Compd.* 549, 46. <https://doi.org/10.1016/j.jallcom.2012.09.050> (2013).
- L. Mao, C. Liu, Y. Gao, X. Han, S. Jiang, and Z. Chen, *Mater. Sci. Eng. A* 701, 7. <https://doi.org/10.1016/j.msea.2017.06.008> (2017).
- F.-S. Pan, J. Zhang, J.-F. Wang, M.-B. Yang, H. En-Hou, and C. Rong-Shi, *Trans. Nonferrous Met. Soc. China* 20, 1249. [https://doi.org/10.1016/S1003-6326\(09\)60287-9](https://doi.org/10.1016/S1003-6326(09)60287-9) (2010).
- G.H. Su, L. Zhang, L.R. Cheng, Y.B. Liu, and Z.Y. Cao, *Trans. Nonferrous Met. Soc. China Engl. Ed.* 20, 383. [https://doi.org/10.1016/S1003-6326\(09\)60150-3](https://doi.org/10.1016/S1003-6326(09)60150-3) (2010).
- J. Wei, J. Chen, H. Yan, B. Su, and X. Pan, *J. Alloys Compd.* 548, 52. <https://doi.org/10.1016/J.JALLCOM.2012.08.102> (2013).

Publisher's Note Springer Nature remains neutral with regard to jurisdictional claims in published maps and institutional affiliations.